Check for updates

Microwave-assisted interzeolite transformations†

Stanislav Ferdov ✱[a,b] and Renato Gonçalves [c]

Microwave heating of FAU zeolite in alkaline solutions results in transformations into EDI, MER, LTJ, CAN, and ANA-type zeolites. The use of microwaves significantly accelerates the synthesis and uncovers a previously unobserved transformation to LTJ-type zeolite.

Zeolites are hydrated aluminosilicates whose active synthesis began in the 1950s, driven by their commercialization in separation and purification processes.[1] Initially, zeolite production has been based on the hydrothermal conversion of aluminosilicate gels. Over time, this method proved effective not only for zeolites but also for a variety of chemically different zeolite-like materials.[2,3] For many years, gel-based synthesis remained the dominant method. However, in the pursuit of faster, more sustainable, and better-controlled synthesis, an alternative technique – interzeolite transformation (IZT) has reemerged, building on the early works of Barrer.[4] The IZT method involves the hydrothermal[5] or room temperature[6] transformation of a pre-existing ("parent") zeolite into a structurally different "daughter" zeolite. This approach has gained significant attention due to its simplicity and potential advantages. These include faster crystallization, the ability to produce frameworks with a high Si/Al ratio and advanced pore chemistry, the creation of hierarchical structures, and the achievement of low synthesis temperatures and short crystallization times—outcomes that are often difficult to reach with conventional gel-based zeolite synthesis.[6–11] Among the parent phases, FAU-type zeolite is one of the most studied due to its wide availability, cost-effective synthesis, and low-density framework, which allows transformations into a range of lower-density zeolites.[12] One such transformation is the conversion of FAU to MER-type zeolite, reported by Kirschhock

and colleagues in 2013.[13] They used an Rb- and Na-containing hydroxide solution and FAU zeolite with a Si/Al ratio of 2.6, obtaining MER zeolite after 96 hours at 95 °C. Similarly, Chengyu *et al.* later reported the synthesis of MER zeolite by transforming NaY and HY-FAU (Si/Al = 2.4–2.6) zeolites in a K-containing solution at 100–150 °C for 96 hours.[14] MER zeolite was obtained under dry conditions by the mechano-chemical treatment of FAU zeolite (Si/Al = 2.4) with KOH at 110 °C for 120 minutes.[15] Additionally, MER has been synthesized from clinoptilolite-rich natural zeolite.[16] EDI zeolite, another potassium-containing zeolite, was recently synthesized by IZT of FAU in concentrated KOH solutions, either at room temperature for 11–35 days or at 60 °C for 6–27 hours.[6] The IZT resulting in ANA-type structures was reported in 1999 by Chiyoda and Davis, who transformed NaY (Si/Al = 2.0–3.0) into ANA zeolite using sodium-containing solutions.[17] In 2010, Wang *et al.* synthesized ANA zeolite crystals with a regular icositetrahedron morphology by transforming ultrastable zeolite Y (Si/Al = 6.7) in NaOH solution at 100 °C for 42–288 hours.[18] In 2013, Kirschhock and colleagues synthesized synthetic pollucite (Cs-ANA) by IZT of FAU zeolite (Si/Al = 2.6) in CsOH solution at 95 °C for 48 hours[13] More recently, ANA zeolite was synthesized through mechanochemically-assisted transformation of commercial FAU (Si/Al = 2.4) using CsOH or NaOH at 110 °C for 120 minutes.[15] CAN zeolite was also synthesized under similar conditions using KOH.[15] Notably, the mechanochemically-assisted transformations of FAU are faster than the conventional synthesis of MER and ANA, which typically take 6 hours[19] and 5–10 hours,[20] respectively.

Considering the need for more efficient synthesis routes, various types of radiation, such as UV light,[21,22] gamma rays[23] and microwaves,[24–26] have been used to enhance the zeolite crystallization from gel media. However, similar methods have not yet been applied to IZT-based synthesis. In this context, this work introduces the first examples of microwave-assisted interzeolite transformation and shows how this method can significantly accelerate crystallization and uncover new transformation pathways.

a Physics Centre of Minho and Porto Universities (CF-UM-UP), University of Minho, 4710-057 Braga, Portugal. E-mail: sferdov@fisica.uminho.pt
b Laboratory of Physics for Materials and Emergent Technologies, LaPMET, University of Minho, 4710-057 Braga, Portugal
c Chemistry Centre of the University of Minho (CQ-UM), 4710-057 Braga, Portugal

Fig. 1 shows the indexed powder XRD patterns of **EDI** zeolites (PDF: 025-0619) obtained by the transformation of **FAU** zeolite under the conditions listed in Table 1. At 160 °C, the **EDI** zeolite crystallizes within 10 minutes, while it takes 65 minutes at 80 °C and 365 minutes at 60 °C. At 60 °C, a longer crystallization time (1325 minutes) results in **EDI** zeolite with higher relative XRD peaks intensity. However, at 80 °C and 160 °C, the thermodynamic stability of **EDI** zeolite is reduced, and longer synthesis times lead to the formation of a dense **KAlSiO₄** phase (Fig. S1†).

Fig. 2a shows the transformation of **FAU** to **MER** zeolite followed by powder XRD (indexed by PDF: 01-086-1110) at different temperatures for 15 minutes of synthesis with batch composition: 0.5–1 g **FAU**–1 g KOH–4.5 g H_2O. The parent **FAU** structure is maintained at 130 °C and 140 °C, but there is an apparent shift of framework-dependent XRD reflections (in the 20–35°2θ range) towards smaller angles. Especially indicative is the atomic plane (555). The refined powder XRD patterns (Fig. S2 and S3†) of **FAU** obtained at 130 °C show unit cell of a = 24.94 Å, and FAU obtained at 140 °C shows unit cell a = 24.91 Å that, according to Breck–Flanigen equation [Si/Al = $((192 \times 0.00868)/(a_0 - 24.191)) - (1)]^{27}$ corresponds to a Si/Al ratio of 1.2 and 1.3, respectively. These values are slightly lower than those determined by EDS analyses (1.7), suggesting the presence of an amorphous phase. This amorphous phase is formed during the desilication of **FAU** zeolite in alkaline solution, where silicon is preferentially removed from the framework due to the higher susceptibility of Si–O–Si bonds to alkaline hydrolysis, while aluminium tends to remain in the structure. This selective removal of silicon can lead to localized framework degradation and the formation of amorphous, silicon-rich aluminosilicate regions. As a result, bulk analysis by EDS, which captures both crystalline and amorphous components, shows a higher Si/Al ratio (*e.g.*, 1.7), while XRD, which only reflects the composition of the remaining crystalline FAU framework, shows a lower Si/Al ratio (*e.g.*, 1.3). This discrepancy indicates that desilication has introduced noncrystalline, Si-rich amorphous material, and that the crystalline fraction of the zeolite has become relatively Al-enriched. These observations suggest that the early stages of interzeolite transformation not only alter the chemical composition but also result in partial amorphization and framework reconstruction, which cannot be fully captured by XRD alone. The lowest temperature at which **MER** zeolite crystallizes is 150 °C. Despite the doubled amount of **FAU** seeds at 160 °C, **MER** zeolite also forms and shows a higher relative peak intensity compared to the **MER** obtained at 150 and 170 °C, suggesting an improved crystallinity (Fig. 2a).

Fig. 2b shows the transformation of **FAU** zeolite to **LTJ** zeolite (PDF: 01-080-3851) followed by XRD. This transformation occurs in the system 0.15 g **FAU**–1 g KOH–4.5 g H_2O at 160 °C for 15 minutes. The difference with the **FAU**–**MER** zeolite transformation is the lower amount of **FAU** seeds, which apparently influence the phase selectivity in the studied system. To the best of our knowledge, **LTJ** has not yet been synthesized *via* IZT. Typical **LTJ** synthesis includes synthesis from rice husk[28] or kaolinite[29] at hydrothermal conditions, which takes more than 24 hours.

Fig. 3 shows the powder XRD patterns following the transformation of **FAU** to **ANA** and **FAU** to **CAN** zeolites. The **FAU**–**ANA** IZT was achieved at the system: 0.5 g **FAU**–1.36 g CsOH–2.59 g H_2O (at 170 °C for 65 minutes), resulting in **Cs-ANA** with a Si/Al ratio of 3.3 (Fig. 3b). A similar **FAU**–**ANA** (Si/Al = 2.6) transformation occurred at 0.5 g **FAU**–0.71 g CsOH–3.5 g H_2O (at 160 °C for 15 minutes) (Fig. 3c) leading to XRD patterns with higher relative crystallinity. These results demonstrate that both the framework composition and crystallinity can be effectively controlled by adjusting the synthesis conditions. **CAN** zeolite was synthesized at 0.5 g **FAU**–1 g NaOH–
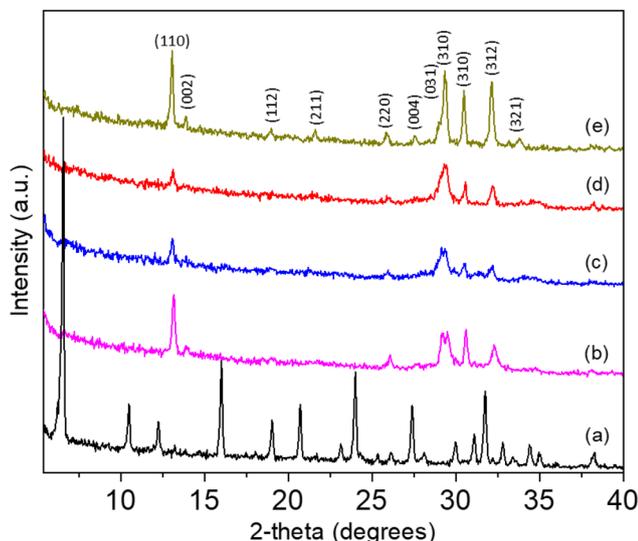

Fig. 1 Powder XRD pattern showing the transformation of the (a) parent **FAU** zeolite into **EDI** zeolite at (b) 160 °C for 10 minutes (no. 11), (c), 80 °C for 65 minutes (no. 3), (d) 60 °C for 365 minutes (no. 2) and (e) 60 °C for 1325 minutes (no. 1).

Table 1 Synthesis conditions leading to ITZ of **FAU** to **EDI**, **MER**, **LTJ**, **ANA**, and **CAN** zeolites

No	Temp (°C)	FAU (g)	KOH (g)	H₂O (g)	Time (min)	Daughter Phase	Si/Al EDS
1	60	0.5	4.47	3.9	1325	**EDI**	1.2
2	80	0.5	4.47	3.9	365	**EDI**	1.2
3	80	0.5	4.47	3.9	65	**EDI**	1.3
4	130	0.5	1	4.5	15	**FAU**	1.7
5	140	0.5	1	4.5	15	**FAU**	1.7
6	150	0.5	1	4.5	15	**MER**	1.7
7	160	0.5	1[a]	4.5	15	**CAN**	1.2
8	160	0.15	1	4.5	15	**LTJ**	1.3
9	160	1	1	4.5	15	**MER**	1.8
10	160	0.5	0.71[b]	3.5	15	**Cs-ANA**	2.6
11	160	0.5	1	2	10	**EDI**	1.3
12	170	0.5	1	4.5	15	**MER**	1.8
13	170	0.5	1.35[b]	2.59	65	**Cs-ANA**	3.3

[a] NaOH. [b] CsOH.
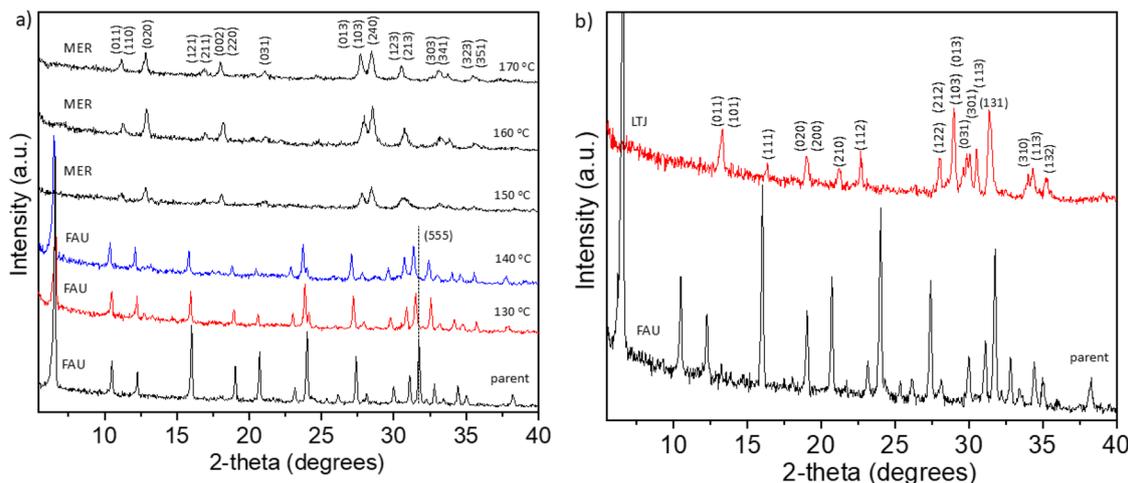
Fig. 2 Powder XRD patterns of zeolites obtained by IZT of (a) parent **FAU** sample for 15 minutes at different temperatures – dashed line shows the shift of (555) reflection of the parent **FAU** sample with increasing temperature of synthesis. (b) Powder XRD patterns of transformation of **FAU** to **LTJ** zeolite at 160 °C for 15 minutes.
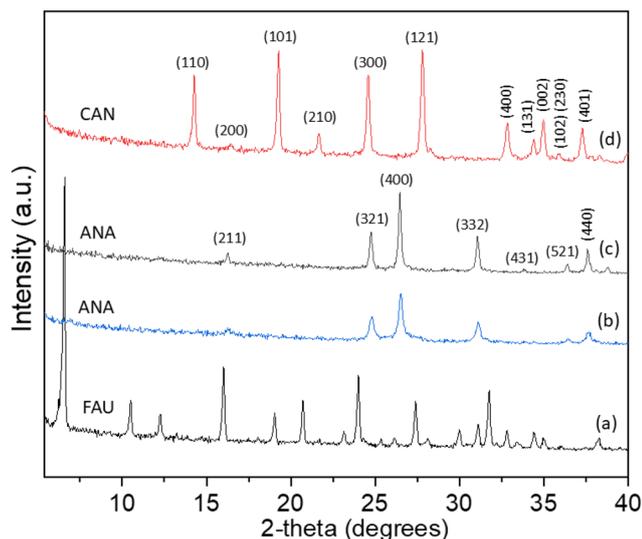
Fig. 3 Powder XRD patterns of transformation of (a) **FAU** to (b) **ANA** zeolite obtained at 170 °C for 65 minutes. (c) **ANA** zeolite obtained at 160 °C for 15 minutes. (d) **CAN** zeolite obtained at 160 °C for 15 minutes.

3.9 g H_2O (160 °C for 15 minutes), resulting in a framework with a Si/Al ratio of 1.2 (Fig. 3d).

Fig. 4a outline the **FAU–FAU**, **FAU–EDI**, **FAU–MER**, **FAU–LTJ**, **FAU–ANA** and **FAU–CAN** interzeolite transformations, along with their respective temperatures and corresponding Si/Al ratios. Except for the **FAU–FAU** transformation, none of the interzeolite transformations (IZTs) exhibit common composite building units (CBUs) between the parent **FAU** and the resulting daughter zeolite (Fig. S4†). This suggests that the transformation likely involves a complete breakdown of the parent zeolite framework into amorphous or intermediate species

before reconstruction into the daughter phase. Along with powder XRD diffraction, these transformations were followed by FTIR spectroscopy (Fig. 4b). All samples show different intensity bands between 400 and 800 cm^{-1} associated with the secondary building units of the zeolite framework, reflecting differences in framework topology.[30] A comparison of the spectra reveals clear differences in the framework structures of the various zeolites. These differences are particularly evident in the positions of the absorption bands associated with asymmetric Si–O–T (T = Si or Al) vibrations. In particular, variations in the position of the intense bands around 950–1090 cm^{-1} reflect both differences in the Si/Al ratio and changes in the local environment within the framework.[30,31] Generally, the position of the most intense band in the asymmetric stretching region shifts toward lower wavenumbers with decreasing Si/Al ratio, as observed: $FAU_{Si/Al=3}$ (991 cm^{-1}), $ANA_{Si/Al=2.6}$ (986 cm^{-1}), $MER_{Si/Al=1.8}$ (977 cm^{-1}), $FAU_{Si/Al=1.7}$ (966 cm^{-1}), $LTJ_{Si/Al=1.3}$ (952 cm^{-1}), $EDI_{Si/Al=1.3}$ (956 cm^{-1}), $CAN_{Si/Al=1.2}$ (960 cm^{-1}). The only exceptions to this trend are **LTJ**, **EDI**, and **CAN**, where the differences in Si/Al ratio are minimal. This deviation may be attributed to framework-specific structural features or local compositional effects that influence the vibrational environment independently of the Si/Al ratio.[30]

Fig. 5a–i shows SEM images of the parent **FAU** zeolite and the different daughter zeolites. When the IZT is performed at 130–140 °C, the parent **FAU** zeolite partly dissolves (Fig. 5b, S5, and S6†). This dissolution retains the original particle shape but produces numerous nanofins (100–500 nm) carved into the surface. Compared to previous examples of post-synthetic treatment of **FAU** and other zeolites that result in hierarchal structures,[10,32,33] the microwave-assisted approach shows potential for more simple (organic-free) and faster crystal hierarchization. Between 150 and 170 °C, **FAU** transforms to prismatic intergrowths of **MER** crystals (Fig. 5c and S7†) with Si/Al = 1.7–1.8. The crystals obtained at higher temperatures
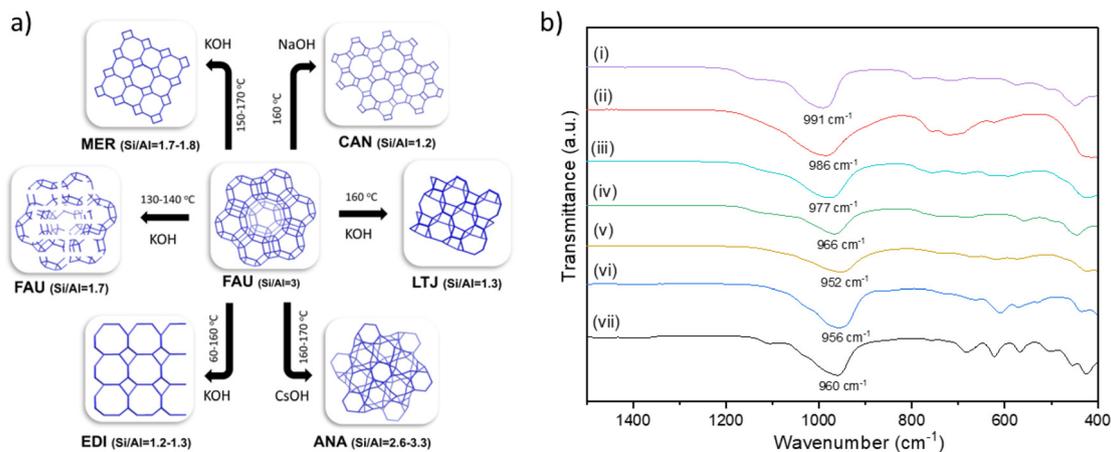
Fig. 4 (a) Schematic presentation of the observed IZT. (b) FTIR spectra of (i) **FAU** Si/Al = 3, (ii) **ANA** Si/Al = 2.6, (iii) **MER** Si/Al = 1.8, (iv) **FAU** Si/Al = 1.7, (v) **LTJ** Si/Al = 1.3, (vi) **EDI** Si/Al = 1.2, (vii) **CAN** Si/Al = 1.2.
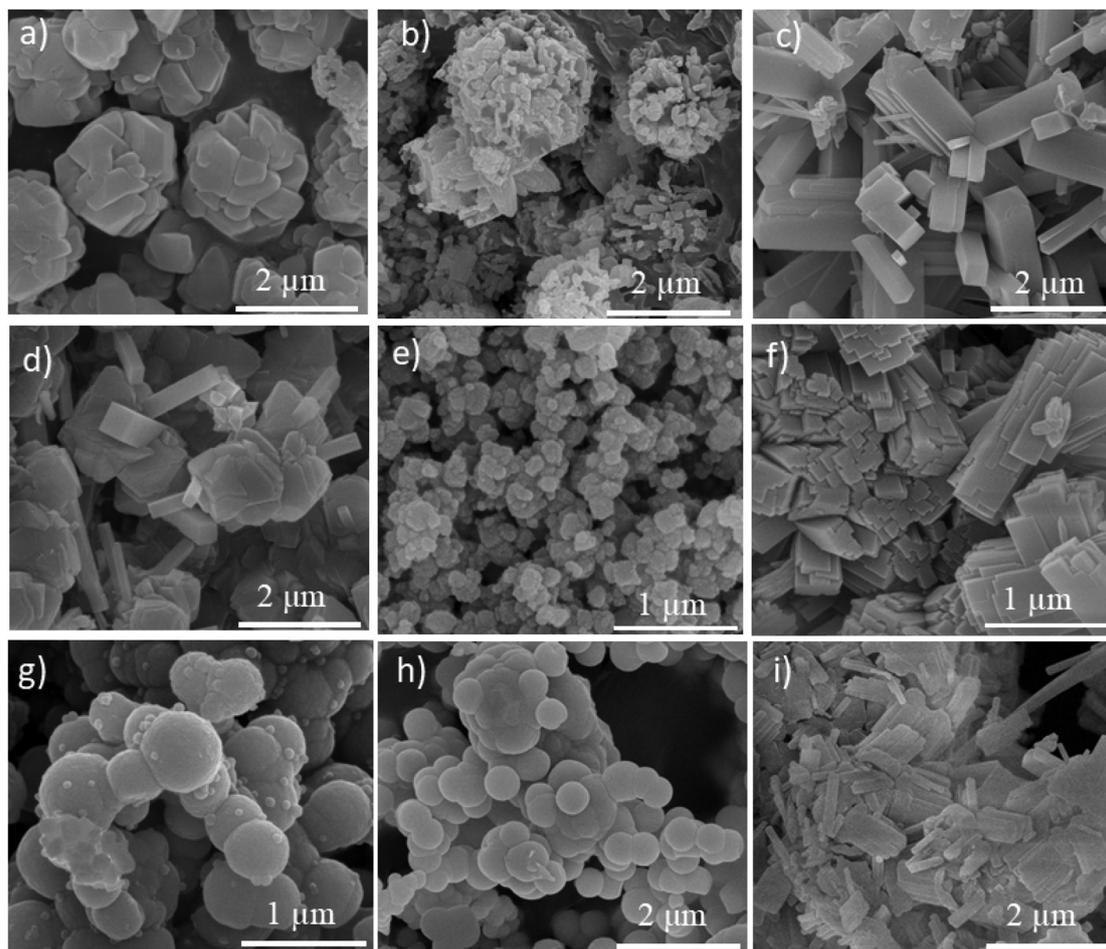

Fig. 5 Representative SEM images of the (a) parent **FAU** zeolite transformed in the conditions listed in Table 1 to (b) **FAU** (no. 4, 5), (c) **MER** (no. 13), (d) **LTJ** (no. 8), (e) **EDI** (no. 1, 2) and (f) **EDI** (no. 11), (g) **Cs-ANA** (no. 14), (h) **Cs-ANA** (no. 10) and (i) **CAN** (no. 7).

(170 °C) are better faced than those obtained at lower temperatures (150–160 °C). **LTJ** zeolite crystallizes as prismatic, well-faced submicron crystals grown over micron-sized particles (Fig. 5d and S8†). Similar prismatic morphology for **LTJ** zeolite has been observed in conventional synthesis.[28,29] EDS chemical analysis on both crystal morphologies showed Si/Al close to

Table 2 Comparison of the time and temperature of selected interzeolite transformations of **FAU** zeolite

IZT	Heating	Time	Temp ($^\circ$C)	Ref.
FAU → **MER**	Conventional	4 d	95	13
FAU → **Cs-ANA**	Conventional	2 d	95	13
FAU → **EDI**	Conventional	6 h	60	6
FAU → **Na-ANA**	Conventional & MC	2 h	110	15
FAU → **Cs-ANA**	Conventional & MC	2 h	110	15
FAU → **MER**	Conventional & MC	2 h	110	15
FAU → **ANA**	Conventional & MC	2 h	110	15
FAU → **CAN**	Conventional & MC	2 h	110	15
FAU → **KAlSiO$_4$**[a]	Microwave	15 min	160	This work
FAU → **MER**	Microwave	15 min	150–170	This work
FAU → **LTJ**	Microwave	15 min	160	This work
FAU → **Cs-ANA**	Microwave	15 min	160	This work
FAU → **EDI**	Microwave	10 min	160	This work
FAU → **CAN**	Microwave	15 min	160	This work

MC – mechanochemical. [a] Feldspathoid[40,41]

1.3. Fig. 5e shows SEM images of **EDI** zeolite obtained in the system 0.5 g **FAU**–4.47 g KOH–3.9 g H$_2$O for 1325 minutes at 60 °C and for 65 minutes at 80 °C, as shown in Fig. S7.† In both synthesis temperatures, **EDI** forms aggregates of nanoparticles (90–100 nm). When synthesized using lower KOH and H$_2$O amounts (0.5 g **FAU**–1 g KOH–2 g H$_2$O) at 160 °C, **EDI** appears as well-formed, intergrown prismatic particles ranging from submicron to micrometer sizes (0.5–1.7 μm) (Fig. 5f). These morphologies are typical of **EDI** zeolite, as previously reported under both room-temperature[6] and classical hydrothermal synthesis.[34–36] **Cs-ANA** zeolites were synthesized under two different conditions: (1) 170 °C for 65 minutes (0.5 g **FAU**–1.35 g CsOH–2.59 g H$_2$O) (Fig. 5g) and (2) 160 °C for 15 minutes (0.5 g **FAU**–0.71 g CsOH–3.5 g H$_2$O) (Fig. 5h). In both cases, **Cs-ANA** crystallizes as aggregates of submicron, sphere-like particles. In the first system, the submicron (400–600 nm) particles are decorated with second-generation nanoparticles (50–70 nm), indicating a decrease in precursor concentration, leading to slower growth and smaller second-generation crystals. This feature is absent in the second CsOH concentrated system, where spherical particles of around 500 nm are formed. Spherical particles of **Cs-ANA** zeolite have been previously described for interzeolite[15] and conventional synthesis.[37] The Si/Al ratio of the sample obtained for 65 minutes is 3.3, while the Si/Al ratio of the sample obtained for 15 minutes is 2.6, indicating a potential for controlling the chemical composition of **Cs-ANA** zeolite. Additionally, in a system of 0.5 g **FAU**–1 g NaOH–4.5 g H$_2$O, **FAU** zeolite transforms into a **CAN**-type structure at 160 °C in 15 minutes (Fig. 5i). The resulting phase crystallizes as sub to micrometric intergrowths of prismatic crystals, which is typical for **CAN**-type zeolites.[38]

Table 2 compares the fastest reported IZTs leading to **EDI**, **MER**, **LTJ**, **ANA**, and **CAN** zeolites with the phases synthesized in this work. In addition, microwave radiation allows **FAU**–**LTJ** transformation, which has not been reported so far. The comparison shows that microwave-assisted synthesis at higher temperatures assures dramatically faster crystallization than the mechanochemically-assisted and the typical conventional heating approach. A non-zeolitic aluminosilicate with a kaliophilite (**KAlSiO$_4$**) structure was also obtained.

In perspective, microwave heating significantly accelerates IZT by introducing two key effects: selective volumetric heating and enhanced dissolution–recrystallization dynamics. Unlike conventional heating, microwaves interact directly with polar molecules and ions, enabling uniform and rapid heating throughout the reaction medium.[39] This promotes faster dissolution of the parent zeolite and accelerates nucleation and framework reorganization. The increased mobility of species under microwave conditions lowers energy barriers and drives more efficient transformation *via* the dissolution–recrystallization mechanism. Additionally, microwave-assisted synthesis can guide the transformation pathway toward the formation of the desired zeolite phase by favouring kinetic over thermodynamic control, reducing the likelihood of competing or metastable phases.

In summary, this work introduces microwave radiation in the synthesis of zeolites by interzeolite transformation. This approach provides control over the particle size and fast access to zeolite structures such as **EDI**, **MER**, **LTJ**, **ANA**, and **CAN**. Additional derivates of the microwave-assisted IZT are the discovery of **FAU**–**LTJ** interzeolite transformation and a pathway to nanostructured faujasites by desilication of a parent zeolite in a short time. From this perspective, further development of the microwave-assisted IZT is expected to result in other zeolite framework types.

Data availability

The data underlying this study are available in the article and its ESI.†

Conflicts of interest

There are no conflicts to declare.

Acknowledgements

References

1 A. J. Mallette, K. Shilpa and J. D. Rimer, *Chem. Rev.*, 2024, **124**, 3416–3493.

2 S. Ferdov, B. Shivachev, I. Koseva, P. Petrova, N. Petrova, R. Titorenkova and R. Nikolova, *Chem. Eng. J.*, 2024, **492**, 152355.

3 J. Rocha and M. W. Anderson, *Eur. J. Inorg. Chem.*, 2000, 801–818.

4 R. Barrer, L. Hinds and E. White, *J. Am. Soc.*, 1953, 1466–1475.

5 T. Sano, M. Itakura and M. Sadakane, *J. Jpn. Pet. Inst.*, 2013, **56**, 183–197.

6 S. Ferdov, *Molecules*, 2024, **29**, 1744.

7 J. Devos, S. Robijns, C. Van Goethem, I. Khalil and M. Dusselier, *Chem. Mater.*, 2021, **33**, 2516–2531.

8 R. Jain, A. J. Mallette and J. D. Rimer, *J. Am. Chem. Soc.*, 2021, **143**, 21446–21460.

9 P. Pornsetmetakul, F. J. A. G. Coumans, J. M. J. J. Heinrichs, H. Zhang, C. Wattanakit and E. J. M. Hensen, *Chem. – Eur. J.*, 2024, **30**, e202302931.

10 M. J. Mendoza-Castro, E. De Oliveira-Jardim, N.-T. Ramírez-Marquez, C.-A. Trujillo, N. Linares and J. García-Martínez, *J. Am. Chem. Soc.*, 2022, **144**, 5163–5171.

11 J. C. Barbosa, D. M. Correia, M. Salado, R. Gonçalves, S. Ferdov, V. de Zea Bermudez, C. M. Costa and S. Lanceros-Mendez, *Adv. Eng. Mater.*, 2022, **25**, 2200849.

12 D. V. Bruter, V. S. Pavlov and I. I. Ivanova, *Pet. Chem.*, 2021, **61**, 251–275.

13 L. Van Tendeloo, E. Gobechiya, E. Breynaert, J. A. Martens and C. E. A. Kirschhock, *Chem. Commun.*, 2013, **49**, 11737–11739.

14 H. W. Yan Chengyu and X. Ruren, *Acta Chim. Sin.*, 2017, **75**, 679–685.

15 N. Jakupec, K. J. Ardila-Fierro, V. Martinez, I. Halasz, J. Volavšek, G. Algara-Siller, M. Etter, V. Valtchev, K. Užarević and A. Palčić, *ACS Sustainable Chem. Eng.*, 2024, **12**, 5220–5228.

16 N. K. Pérez González, D. Díaz Guzmán, M. Vargas Ramírez, F. Legorreta García, E. A. Chávez Urbiola, L. E. Trujillo Villanueva and M. Ramírez Cardona, *Bol. Soc. Esp. Ceram. Vidrio*, 2024, **63**, 279–293.

17 O. Chiyoda and M. E. Davis, *Microporous Mesoporous Mater.*, 1999, **32**, 257–264.

18 Y. Wang, X. Li, Z. Xue, L. Dai, S. Xie and Q. Li, *J. Phys. Chem. B*, 2010, **114**, 5747–5754.

19 Z. Hu, B. Zhao, S. Zhang, Z. Tan, X. Liu and J. Cao, *Microporous Mesoporous Mater.*, 2019, **281**, 75–83.

20 D. Novembre and D. Gimeno, *Sci. Rep.*, 2021, **11**, 13373.

21 S. Ferdov, J. Marques, C. J. Tavares, Z. Lin, S. Mori and N. Tsunoji, *Microporous Mesoporous Mater.*, 2022, **336**, 111858.

22 D. Shi, L. Xu, P. Chen, T. Ma, C. Lin, X. Wang, D. Xu and J. Sun, *Chem. Commun.*, 2019, **55**, 1390–1393.

23 X. Chen, M. Qiu, S. Li, C. Yang, L. Shi, S. Zhou, G. Yu, L. Ge, X. Yu, Z. Liu, N. Sun, K. Zhang, H. Wang, M. Wang, L. Zhong and Y. Sun, *Angew. Chem., Int. Ed.*, 2020, **59**, 11325–11329.

24 T. Yoshioka, Z. Liu, K. Iyoki, A. Chokkalingam, Y. Yonezawa, Y. Hotta, R. Ohnishi, T. Matsuo, Y. Yanaba, K. Ohara, T. Takewaki, T. Sano, T. Okubo and T. Wakihara, *React. Chem. Eng.*, 2021, **6**, 74–81.

25 Z. Ma, H. Deng, L. Li, Q. Zhang, G. Chen, C. Sun, H. He and J. Yu, *Chem. Sci.*, 2023, **14**, 2131–2138.

26 B. Panzarella, G. A. Tompsett, K. S. Yngvesson and W. C. Conner, *J. Phys. Chem. B*, 2007, **111**, 12657–12667.

27 D. Breck and J. Smith, *Sci. Am.*, 1959, **200**, 85–96.

28 E.-P. Ng, G. K. Lim, G.-L. Khoo, K.-H. Tan, B. S. Ooi, F. Adam, T. C. Ling and K.-L. Wong, *Mater. Chem. Phys.*, 2015, **155**, 30–35.

29 S. M. Kamyab and C. D. Williams, *Microporous Mesoporous Mater.*, 2021, **318**, 111006.

30 E. M. Flanigen, H. Khatami and H. A. Szymanski, in *Molecular Sieve Zeolites-I*, American Chemical Society, 1974, ch. 16, vol. 101, pp. 201–229.

31 Y.-K. Ma, S. Rigolet, L. Michelin, J.-L. Paillaud, S. Mintova, F. Khoerunnisa, T. J. Daou and E.-P. Ng, *Microporous Mesoporous Mater.*, 2021, **311**, 110683.

32 D. Verboekend, N. Nuttens, R. Locus, J. Van Aelst, P. Verolme, J. C. Groen, J. Pérez-Ramírez and B. F. Sels, *Chem. Soc. Rev.*, 2016, **45**, 3331–3352.

33 D. Verboekend, G. Vilé and J. Pérez-Ramírez, *Adv. Funct. Mater.*, 2012, **22**, 916–928.

34 T. Matsumoto, T. Miyazaki and Y. Goto, *J. Eur. Ceram. Soc.*, 2006, **26**, 455–458.

35 A. Chawla, A. J. Mallette, R. Jain, N. Le, F. C. Robles Hernández and J. D. Rimer, *Microporous Mesoporous Mater.*, 2022, **341**, 112026.

36 S.-F. Wong, H. Awala, A. Vincente, R. Retoux, T. C. Ling, S. Mintova, R. R. Mukti and E.-P. Ng, *Microporous Mesoporous Mater.*, 2017, **249**, 105–110.

37 N. Pellens, N. Doppelhammer, K. Asselman, B. Thijs, B. Jakoby, E. K. Reichel, F. Taulelle, J. Martens, E. Breynaert and C. E. A. Kirschhock, *Faraday Discuss.*, 2022, **235**, 162–182.

38 I. I. Amin, A. W. Wahab, R. R. Mukti and P. Taba, *Appl. Nanosci.*, 2023, **13**, 5389–5398.

39 X. Zeng, X. Hu, H. Song, G. Xia, Z.-Y. Shen, R. Yu and M. Moskovits, *Microporous Mesoporous Mater.*, 2021, **323**, 111262.

40 J. Yuan, H. Ma, Z. Luo, X. Ma and Q. Guo, *Minerals*, 2021, **11**, 36.

41 E. Mugnaioli, E. Bonaccorsi, A. E. Lanza, E. Elkaim, V. Diez-Gómez, I. Sobrados, M. Gemmi and M. Gregorkiewitz, *IUCrJ*, 2020, **7**, 1070–1083.